Ekman decay of a dipolar vortex in a rotating fluid

L. Zavala Sansón,[a] G. J. F. van Heijst, and N. A. Backx
Fluid Dynamics Laboratory, Eindhoven University of Technology, P. O. Box 513, 5600 MB, Eindhoven, The Netherlands

(Received 4 January 2000; accepted 3 November 2000)

The evolution of quasi-two-dimensional (2D) dipolar vortices over a flat bottom in a rotating fluid system is studied numerically, and the main results are experimentally verified. Our aim is to examine the dipole decay due to bottom friction effects. The numerical simulations are based on the 2D physical model derived by Zavala Sansón and van Heijst [J. Fluid Mech. **412**, 75 (2000)], which contains nonlinear Ekman terms, associated with bottom friction, in the vorticity equation. In contrast, the conventional 2D model with bottom friction only retains a linear stretching term in the same equation. It is shown that the dipole trajectory is deflected towards the right (i.e., in the anticyclonic direction) when nonlinear Ekman terms are included. This effect is not observed in simulations based on the conventional model, where the dipole trajectory is a straight line. The basic reason for this behavior is the slower decay of the anticyclonic part of the dipole, with respect to the cyclonic one, due to nonlinear Ekman effects. Another important result is the exchange of fluid between the cyclonic part and the ambient, leaving a tail behind the dipole. By means of laboratory experiments in a rotating tank, these results are qualitatively verified. [DOI: 10.1063/1.1335541]

I. INTRODUCTION

The emergence of two-dimensional (2D) structures is a common phenomenon observed in rotating flows with low Rossby number (i.e., where rotation effects are dominant). For instance in geophysical fluid dynamics, where the Earth's rotation plays a crucial role, such structures are frequently observed. These features can also be found in laboratory experiments in a rotating fluid tank. Obviously, in these examples the motion is not purely 2D because of the influence of several factors, e.g., bottom friction, stratification, free-surface effects, etc. The 2D motion, however, is predominant and can appropriately be called ''quasi-2D.''

The quasi-2D flows considered here are those affected by bottom friction, associated with the no-slip boundary condition at the solid bottom. For the case of a homogeneous fluid the motion in the interior domain, i.e., outside the thin Ekman layer at the bottom, is predominantly 2D. The Ekman layer induces a weak vertical motion in the interior flow (the so-called Ekman suction/blowing), which eventually affects its evolution. This is the basic mechanism of bottom friction. The smallness of such effects allows their incorporation in 2D models. The well-known conventional 2D model with bottom friction includes a linear term in the vorticity evolution equation, together with lateral viscous effects. In a recent study, Zavala Sansón and van Heijst[1] (henceforth ZS00) derived an extended 2D model in the vorticity–stream function formulation including bottom damping effects, which were shown to explain the main characteristics of the evolution of experimental monopolar vortices quite well. The model contains the linear Ekman condition as the bottom boundary condition when the continuity equation is vertically integrated, but nonlinear Ekman effects are incorporated in the vorticity evolution equation, in contrast with the conventional 2D model.

In this paper, the evolution of quasi-2D dipolar vortices in a homogeneous fluid layer over a flat bottom is studied. A dipole consists of two counter-rotating vortices whose mutual interactions provide the self-propelling mechanism. In particular, our aim is to examine the effect of bottom friction in the evolution of such vortices, by means of numerical simulations based on the extended 2D model of ZS00 and the conventional model, together with laboratory experiments in a rotating tank.

The linear Ekman condition used in the 2D models predicts that the vertical velocity induced by the Ekman layer in the interior flow is proportional to the vertical component of the relative vorticity. As a consequence, the pumping (blowing) of fluid from the Ekman layer to the interior flow in the conventional model, represented by a linear term in the vorticity equation, produces an exponential decay of cyclonic (anticyclonic) fluid columns. In other words, linear Ekman friction produces the same effect in cyclones and anticyclones. In contrast, the nonlinear Ekman terms in the extended model break this symmetry. As a result, bottom friction has different effects on fluid columns with positive or negative relative vorticity. In particular, cyclones decay faster than anticyclones.[1,2] Therefore it can be expected that the trajectory of a dipolar vortex, when affected by bottom friction, will be deflected to the right (i.e., in an anticyclonic sense) due to the faster decay of its cyclonic half. This is one of the main results shown in this study. Another important

[a]Present address: Department of Physical Oceanography, CICESE, Km 107 Carretera Tijuana Ensenada 22800 Ensenada, BC, México. Phone: (52)(6)-1745050 ext. 24106; fax: (52)(6)-1750568; electronic mail: lzavala@cicese.mx

observation is the ''detrainment'' of fluid from the dipole to the ambient. This leaking effect originates mainly from the cyclonic half. Both phenomena are consequences of nonlinear bottom friction effects. This notion is stressed by the fact that both features are observed in numerical simulations based on the extended model of ZS00, while they are absent in flow simulations carried out with the conventional 2D model.

In the present numerical simulations the Chaplygin–Lamb dipole[3] is used as an initial flow condition. Such a dipole is an exact solution of the inviscid Euler equations. These well-known dipolar structures have been studied before by a number of authors. Nielsen and Juul Rasmussen[4] and van Geffen and van Heijst[5] studied the evolution of Chaplygin–Lamb vortices under the influence of lateral viscous effects (without Ekman damping). In such a case, diffusion of vorticity induces the vortex decay, as well as a slight radial expansion. On the other hand, Swaters and Flierl[6] studied the Ekman dissipation of a barotropic modon by using the conventional linear damping term in the vorticity equation. In that study, lateral viscous effects were not considered. As a result, the dipole decays exponentially and its shape is preserved. What above has been called a ''conventional model'' is in fact a model including lateral viscous effects together with linear Ekman friction. It is worth mentioning that, for the flow regimes studied here, lateral friction is a weaker effect than Ekman friction, i.e., bottom effects are more important for the vortex decay than lateral viscosity.

Dipolar structures in a rotating system have been studied experimentally in different situations. For instance, Velasco Fuentes and van Heijst[7] and Velasco Fuentes *et al.*[8] studied the motion of dipolar vortices on a topographic β-plane; Velasco Fuentes[9] reported the dipole evolution on a γ-plane; Carnevale *et al.*[10] examined the problem of a dipole colliding with a vertical wall on a β-plane. In contrast to those studies, in the present paper we examine the dipole evolution during relatively long periods of time (more than one Ekman period), in order to observe the influence of the bottom in the vortex decay.

The rest of the paper is organized as follows: In Sec. II the viscous 2D physical models, with and without Ekman effects, are presented. Numerical simulations, based on those 2D models, of dipolar vortices over a flat bottom are presented in Sec. III. In Sec. IV, the behavior of a typical experimental dipole is shown, which qualitatively verifies the most important numerical results. Finally, in Sec. V the results are discussed and summarized. The evolution of the Chaplygin–Lamb dipole, using conventional 2D viscous models is analytically described in the Appendix.

II. VISCOUS 2D MODELS

In this section, the 2D model incorporating bottom friction derived by ZS00, together with the conventional formulation used in many other studies, are presented. These models apply to a homogeneous fluid layer over a flat horizontal surface, rotating at a constant angular speed. Using conventional Cartesian coordinates (x,y,z), the angular rotation $\mathbf{\Omega}=(0,0,\Omega)$ is taken anti-parallel to the gravitational acceleration $\mathbf{g}=(0,0,-g)$. The evolution equation in the vorticity–stream function formulation is (henceforth referred to as *model M1*, as in ZS00)

$$\frac{\partial\omega}{\partial t}+J(\omega,\psi)-\frac{1}{2}E^{1/2}\nabla\psi\cdot\nabla\omega = \nu\nabla^2\omega-\tfrac{1}{2}E^{1/2}\omega(\omega+f), \tag{2.1}$$

where $\omega=\partial v/\partial x-\partial u/\partial y$ is the z component of the relative vorticity, (u,v) are the velocity components in the (x,y) directions, respectively, t is the time, ν is the kinematic viscosity, $f=2\Omega$ is the Coriolis parameter, $\nabla^2=\partial^2/\partial x^2+\partial^2/\partial y^2$ is the horizontal Laplacian operator, J is the Jacobian operator, and E is the Ekman number defined by

$$E=\frac{2\nu}{fH^2}, \tag{2.2}$$

where H is the fluid depth. The terms proportional to $E^{1/2}$, which is much smaller than unity, represent the bottom friction effects. The (nonlinear) Ekman terms on the left-hand-side of (2.1) are the corrections to the advective terms $J(\omega,\psi)$ due to bottom friction. The Ekman terms on the right-hand-side represent stretching effects associated with the Ekman pumping. The stream function ψ is related to the relative vorticity through the Poisson equation,

$$\omega=-\nabla^2\psi, \tag{2.3}$$

and the horizontal velocities are

$$u=\frac{\partial\psi}{\partial y}-\frac{1}{2}E^{1/2}\frac{\partial\psi}{\partial x}, \tag{2.4}$$

$$v=-\frac{\partial\psi}{\partial x}-\frac{1}{2}E^{1/2}\frac{\partial\psi}{\partial y}. \tag{2.5}$$

Note that the $O(E^{1/2})$ correction in the horizontal velocities represents a potential flow, since it vanishes when the curl of the velocity field is taken.

The conventional 2D model including bottom damping, used in many previous studies (see, e.g., Pedlosky[11]), only considers the linear part of the Ekman stretching terms in the vorticity equation (hereafter *model M2*):

$$\frac{\partial\omega}{\partial t}+J(\omega,\psi)=\nu\nabla^2\omega-\frac{1}{2}E^{1/2}f\omega. \tag{2.6}$$

Under this approximation, the stream function and the vorticity are related through the Poisson equation (2.3), but the horizontal velocities do not include the correction $O(E^{1/2})$ as in (2.4) and (2.5).

Dropping all the Ekman terms, the purely 2D model (hereafter, *model M3*) is obtained:

$$\frac{\partial\omega}{\partial t}+J(\omega,\psi)=\nu\nabla^2\omega. \tag{2.7}$$

This model was used by Nielsen and Juul Rasmussen[4] and van Geffen and van Heijst,[5] to study the Chaplygin–Lamb dipole evolution only in the presence of lateral viscous effects. Some additional simulations based on M3 will be used

in order to illustrate the effects of Ekman friction obtained with M1 and M2. Note that this equation also applies for a nonrotating system.

Considering only the linear Ekman term, i.e., without lateral viscous effects, the evolution equation is (hereafter, *model M4*)

$$\frac{\partial \omega}{\partial t} + J(\omega, \psi) = -\frac{1}{2} E^{1/2} f \omega. \tag{2.8}$$

Swaters and Flierl[6] studied the evolution of barotropic modons by using an equivalent damping term. Note that model M2 includes both types of viscous effects as contained in models M3 and M4.

III. NUMERICAL SIMULATIONS

The numerical simulations were performed by means of a finite differences code, which was originally developed for purely two-dimensional flows[12,13] and later extended to include variable topography[14,15] or bottom friction (ZS00). The numerical domain is a rectangle of $L_x \times L_y = 150 \times 100$ cm with periodic boundaries discretized by 128×128 grid points; a constant time step $\delta t = 0.1$ s was used in all simulations; the Coriolis parameter is taken to be 1 s^{-1}; the kinematic viscosity is 0.01 $cm^2\ s^{-1}$, and the fluid depth is varied between 8 and 24 cm (these numerical values were chosen corresponding to the laboratory arrangement; see Sec. IV). The duration of the simulations is of order T_E, the Ekman time scale, defined as

$$T_{\mathrm{E}} = \frac{2}{f E^{1/2}} = \left(\frac{2}{f \nu} \right)^{1/2} H. \tag{3.1}$$

For such times, bottom friction effects became manifest. Both in the present laboratory experiments and in geophysical flows, the Ekman time scale is usually much longer than the rotation period of the system. For instance, under typical experimental conditions $E \approx 10^{-4}$, and therefore $T_{\mathrm{E}} \approx 200$ s, while the rotation period of the system is $4\pi/f = 4\pi$ s.

In the numerical simulations the flow is initialized by using the dipolar vortex model discussed by Chaplygin and Lamb[3] which is a solution of the inviscid, steady Euler equations in a reference frame co-moving with the dipole at a constant velocity U. The dipole's interior is characterized by a linear relationship between the relative vorticity and the stream function, i.e., $\omega = k^2 \psi'$ (with ψ' the corrected value of ψ in the co-moving reference frame), where k is a constant, inside a circular region of radius a (the so-called vortex atmosphere). Outside this region the flow is assumed to be irrotational. The relative vorticity distribution in polar coordinates (r, θ) is

$$\omega(r, \theta) = -\frac{2Uk}{J_0(ka)} J_1(kr) \sin\theta, \quad \text{for} \quad 0 \leqslant r \leqslant a, \tag{3.2}$$

and $\omega = 0$ for $r > a$. Here J_0 and J_1 are the first and second order Bessel functions of the first kind, respectively. In the present simulations, the vortex atmosphere is chosen to be $a = 10$ cm, and the initial velocity $U = 1$ cm s^{-1}. Using these values the initial Rossby number $\mathrm{Ro} = U/fa$ is $O(10^{-1})$. In all simulations the vortex was placed at the left side of the domain, at $(x_0, y_0) = (25\ \mathrm{cm}, 50\ \mathrm{cm})$, such that the translation in all the graphs is observed from left to right, along the x direction.

TABLE I. Characteristic parameter values for the simulations of the decaying Chaplygin–Lamb dipole over a flat bottom. The calculation of the Ekman periods is based on $f = 1\ s^{-1}$ and $\nu = 0.01\ cm^2\ s^{-1}$ (the kinematic viscosity of water at 20 °C).

Simulation	Model	H (cm)	T_{E} (s)
1	M1 [Eq. (2.1)]	16	226
2	M2 [Eq. (2.6)]	16	226
3	M3 [Eq. (2.7)]	16	226
4	M4 [Eq. (2.8)]	16	226
5	M1	24	339
6	M1	8	113

The viscous evolution of the Chaplygin–Lamb dipole, using models M2, M3, and M4 is described in the Appendix. Assuming that the dipole maintains its functional form, analytical expressions for the dipole decay, size, speed, energy, and enstrophy can be derived for these models. The same procedure does not apply for model M1, where the linear $\omega - \psi'$ relationship is lost (see below).

Table I lists the numerical simulations performed for this section. First, the evolution of the dipole is studied by means of models M1, M2, M3, and M4 using the same fluid depth (simulations 1, 2, 3, and 4). Later, the influence of the depth is examined by comparing simulations 1, 5, and 6.

A. Dipole trajectory and decay

Figure 1 shows the evolution of the Chaplygin–Lamb dipole calculated with models M1 and M2 (left and right columns, respectively) and using the same depth (simulations 1 and 2 in Table I). Relative vorticity contours are shown for three times during a timespan of approximately $0.88 T_{\mathrm{E}}$. The figure also shows the calculated trajectories of the dipole center for both models (the center is defined as the middle point between the peak vorticities of both halves of the dipole). The main evident feature when using model M1 is that the dipole trajectory is deflected to the right. In contrast, when using the conventional bottom friction formulation, i.e., model M2, the vortex trajectory is a straight line. It must be recalled that without any Ekman effect, i.e., only including lateral viscous effects (model M3), the trajectory is also a straight line.[4,5] The same result applies when only linear Ekman effects (model M4) are considered.[6]

The vortex trajectories are better understood by measuring the positive ω^+ and negative ω^- peak vorticities, which are plotted as a function of time in Fig. 2. Figure 2(a) shows the decay of the peak vorticities when using models M1 (solid line) and M2 (dashed line). The corresponding decays when using models M3 (dashed–dotted line) and M4 (dotted line) are shown in Fig. 2(b). The evolution of the ratio p between the peak vorticities of both halves is shown in the lower row of the same figure. This ratio is defined as

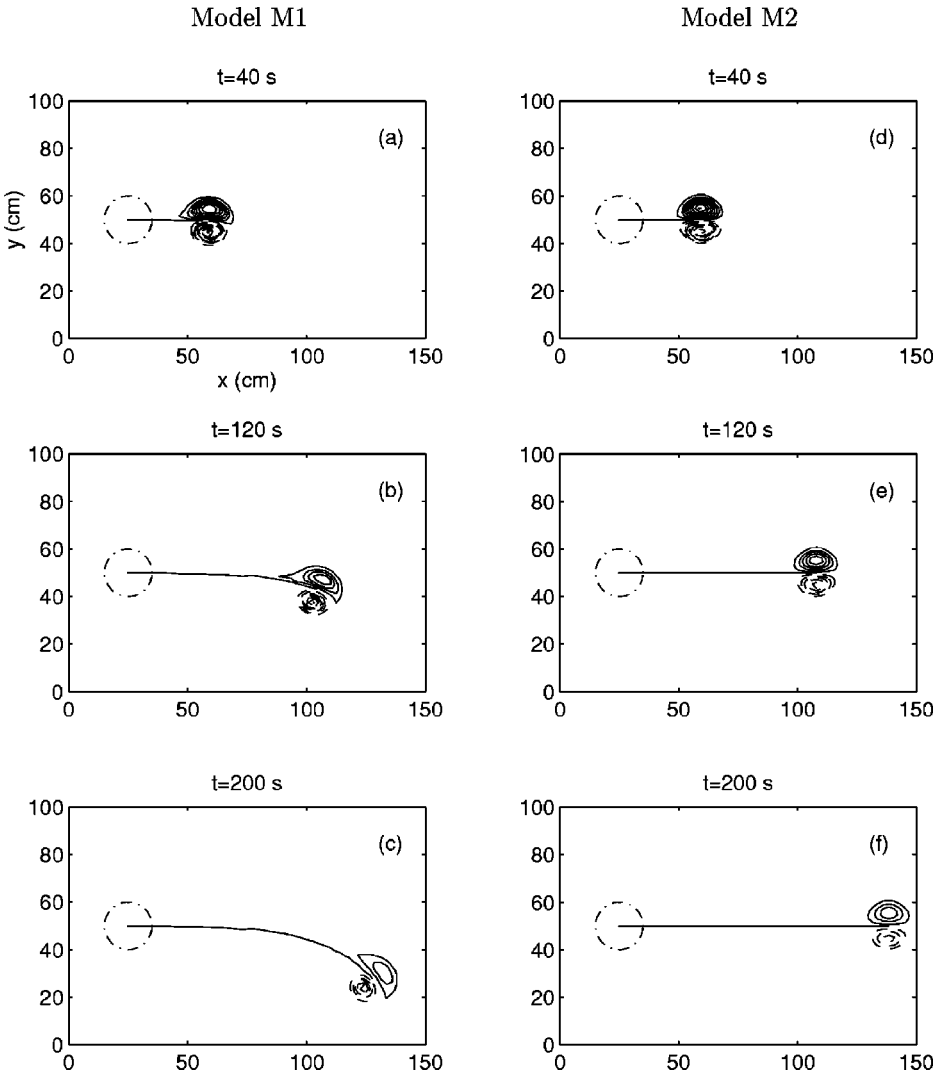

FIG. 1. Vorticity contours of a Chaplygin–Lamb dipole in numerical simulations 1 and 2 (see Table I), based on model M1 [(a)–(c)] and model M2 [(d)–(f)], respectively. The dipole evolution is presented at three different times ($t/T_E=0.18$, 0.53, and 0.88). The contour interval $\Delta\omega$ is 0.1 s^{-1}; solid (dashed) lines are positive (negative) contours. The initial vortex parameters are $(x_0, y_0)=$ (25 cm, 50 cm), $a=10$ cm, $U=1$ cm s^{-1}, $\omega^+(0)=-\omega^-(0)=1.1$ s^{-1}. The dipole trajectory is also shown. The initial atmosphere is indicated by the dashed–dotted circle.

$$p=\frac{\omega^+}{|\omega^-|}. \tag{3.3}$$

When using M1, it is evident that the peak vorticity of the anticyclonic part decays slower than the cyclonic one [Fig. 2(a)]; thus, the ratio p decreases [Fig. 2(c)]. As a consequence, the vortex trajectory is deflected towards the stronger half, i.e., to the right. In contrast, when using model M2 both halves of the dipole decay at the same rate and, therefore, the ratio p remains constant. For this reason, obviously, the trajectory is never deflected. The same occurs when models M3 and M4 are used, but in these cases the peak vorticities decay at a different rate [Figs. 2(b) and 2(d)]. The slowest dipole decay occurs when using model M3, which indicates the smallness of lateral viscous effects compared with Ekman friction. When using model M4 (only linear Ekman friction), the peak vorticities decay exponentially. With model M2 the decay is slightly more pronounced due to the combination of lateral viscous effects and linear Ekman friction. The equations for ω in Table II, derived in the Appendix for models M2, M3, and M4, are in good agreement with the calculated peak vorticities decay.

Note from Fig. 1 that the distance covered by the dipole is not very different when using linear (M2) or nonlinear Ekman friction (M1). Figure 3 shows the velocity components (u_d, v_d) of the dipole center, and the magnitude of its translation velocity $U=(u_d^2+v_d^2)^{1/2}$ as a function of time for the simulations based on M1 and M2 (solid and dashed lines, respectively). The component u_d is slightly smaller when using M1 compared with the simulation based on M2, while v_d is negative for M1 and is obviously zero for M2. However, U is very similar for both cases. The corresponding dipole velocities when using models M3 and M4 have been also included in Fig. 3(b) (dashed–dotted and dotted lines). The evolution of U for models M2, M3, and M4 is well described by the corresponding equations in Table II in the Appendix.

The likeness of the temporal evolution of U when using models M1 and M2, suggests that the energy decay in both models must be similar as well. The kinetic energy is defined as

$$K=\frac{1}{2}\int\int (u^2+v^2)dxdy, \tag{3.4}$$

and the enstrophy as

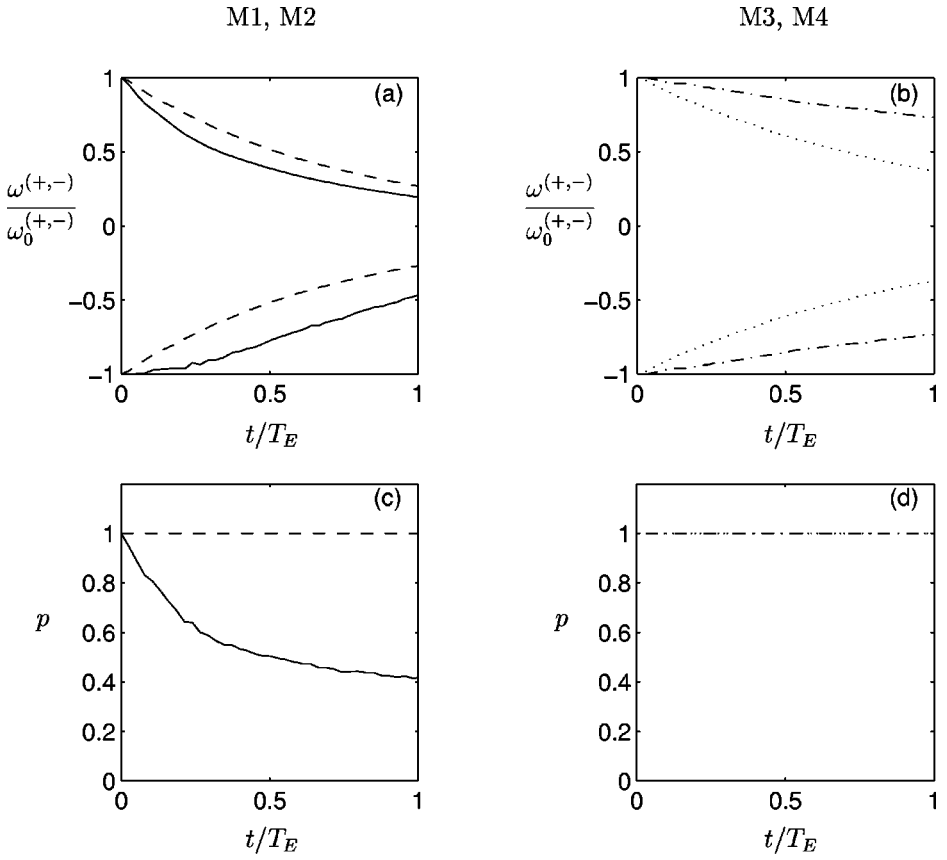

FIG. 2. Upper row: Time evolution of the dipole peak vorticities ω^+ and ω^- in simulations 1, 2, 3, and 4, based on models (a) M1 (solid line) and M2 (dashed line), (b) M3 (dashed–dotted line), and M4 (dotted line). For clarity, simulations 1 and 2 are separated from 3 and 4. Lower row: Time evolution of the ratio $p=\omega^+/|\omega^-|$. (c) and (d) as in the upper row. All values are normalized to unity at $t=0$.

$$S=\frac{1}{2}\int\int \omega^2 dxdy. \tag{3.5}$$

Figure 4 shows the evolution of these ''global'' quantities for the four 2D models. It is evident that with nonlinear Ekman friction (solid line) the energy decay is even slightly slower than with linear Ekman friction (dashed line). Again, expressions for *K* and *S* in Table II in the Appendix describe the energy and enstrophy evolutions for models M2, M3, and M4, very accurately.

In order to investigate the evolution of the relationship between vorticity and stream function, Fig. 5 shows the calculated scatter plots at $t=0.88T_{\mathrm{E}}$ from simulations using models M1 and M2. The stream function has been corrected according to $\psi'=\psi-u_d y+v_d x$ by using the calculated values of u_d and v_d. The simulation based on model M1 [Fig. 5(a)] clearly shows dispersion, and a well-defined functional $\omega-\psi'$ relationship does not exist. The faster decay of the cyclonic part of the dipole is also evident from this figure. In contrast, the dipole evolution according to the simulation using model M2 shows an almost perfectly linear $\omega-\psi'$ relationship [Fig. 5(b)]. This result is further exploited in the Appendix in the analytical treatment of the dipole evolution when using model M2 (as well as models M3 and M4).

B. Advection of passive tracers

Figure 6 shows the transport of passive tracers initially distributed within the dipole in simulations 1 and 2. The panels correspond to the same times as in Fig. 1. At $t=0$ s a

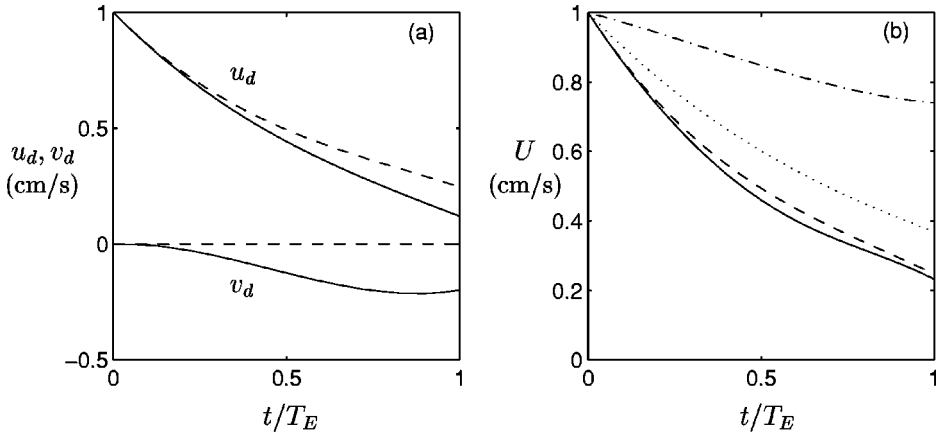

FIG. 3. Calculated (a) velocity components (u_d, v_d) and (b) velocity magnitude *U* of the dipole in simulations 1 and 2, based on models M1 (solid line) and M2 (dashed line), respectively. Panel (b) also shows the velocity magnitude of the dipole from simulations 3 and 4, based on M3 (dashed–dotted line) and M4 (dotted line), respectively.

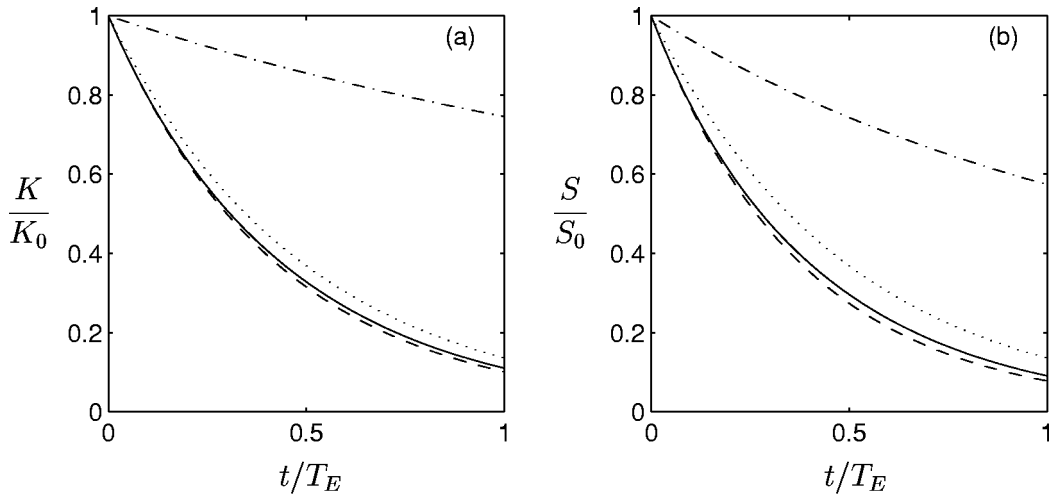

FIG. 4. Calculated (a) energy and (b) enstrophy in simulations 1, 2, 3, and 4, based on models M1 (solid line), M2 (dashed line), M3 (dashed–dotted line), and M4 (dotted line), respectively. All values are normalized to unity at $t=0$.

total of 300 tracers were randomly placed within the dipole's atmosphere, i.e., within a circle of radius $a=10$ cm. Apparently, besides the deflected trajectory, another fundamental feature of the dipole evolution using model M1 is the occurrence of detrainment, i.e., the vortex structure ''leaks'' fluid into the ambient: A tail of tracers is left behind by the translating dipole. In contrast, when using the conventional bottom friction formulation, i.e., model M2, there is no visible advection from the vortex to the ambient fluid. In simulations based on models M3 and M4 the dipole does not leak fluid either (not shown here).

It must be noticed that, when using model M1, the marked fluid parcels left behind in the wake originate from the cyclonic part of the dipole. This asymmetry of the detrainment is more clearly shown in Fig. 7, where the passive tracers in Figs. 6(a)–6(c) are plotted separately for the cyclonic (left column) and the anticyclonic (right column) parts, for three stages of the evolution. This detrainment effect, although rather small, reveals a fundamental difference between models M1 and M2.

C. Vortex decay for different depths

In this subsection the evolution of the same dipolar Chaplygin–Lamb vortex previously shown is studied for different Ekman numbers using model M1. For this purpose the vortex evolution is simulated by using three different depths: 8, 16, and 24 cm, corresponding to simulations 6, 1, and 5 in Table I, respectively.

Figure 8 shows the calculated trajectories of the dipole during a timespan of 180 s. The position of the dipole is defined as in Fig. 1. It is evident that the deflection of the vortex trajectory occurs at earlier times for the lower depth (8 cm). Also, the vortex is able to drift a longer distance for $H=24$ cm, which simply indicates that Ekman effects act more effectively for lower depths. In Fig. 9 the peak vorticities of both halves of the dipole are plotted for the three simulations [Fig. 9(a)], together with the ratio p [Fig. 9(b)]. In all cases the negative half decays slower than the positive one, but the decay is clearly faster for smaller fluid depths.

IV. EXPERIMENTAL DIPOLAR VORTICES

The dipole evolution has been verified qualitatively by means of laboratory experiments in a rotating rectangular tank with horizontal dimensions 150 cm×100 cm. The tank is rotated in the anticlockwise direction at a constant rate of $\Omega=0.5\ \mathrm{s}^{-1}$, which corresponds with a Coriolis parameter $f=2\Omega=1\ \mathrm{s}^{-1}$. Filled with fresh tap water, the tank is set at the specified constant rotation about 30 minutes before the

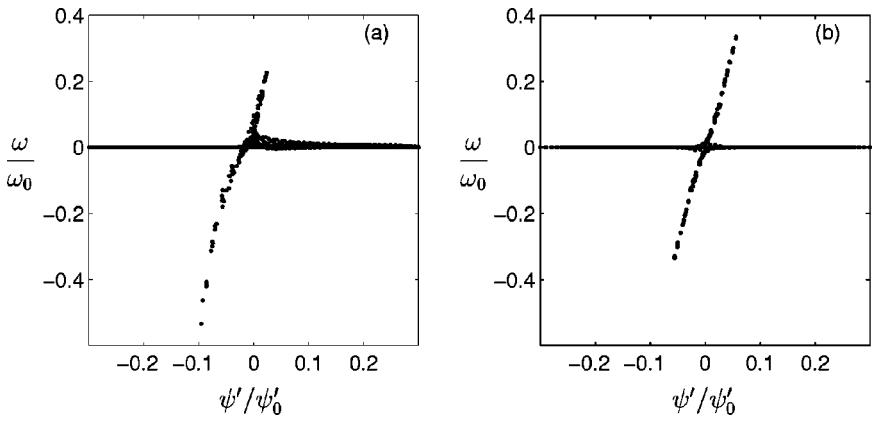

FIG. 5. Numerically calculated scatter plots showing the $\omega-\psi'$ relation representing the dipole evolution at $t=0.88T_{\mathrm{E}}$. (a) Simulation 1 (model M1) and (b) simulation 2 (model M2). All values are normalized to unity at $t=0$.

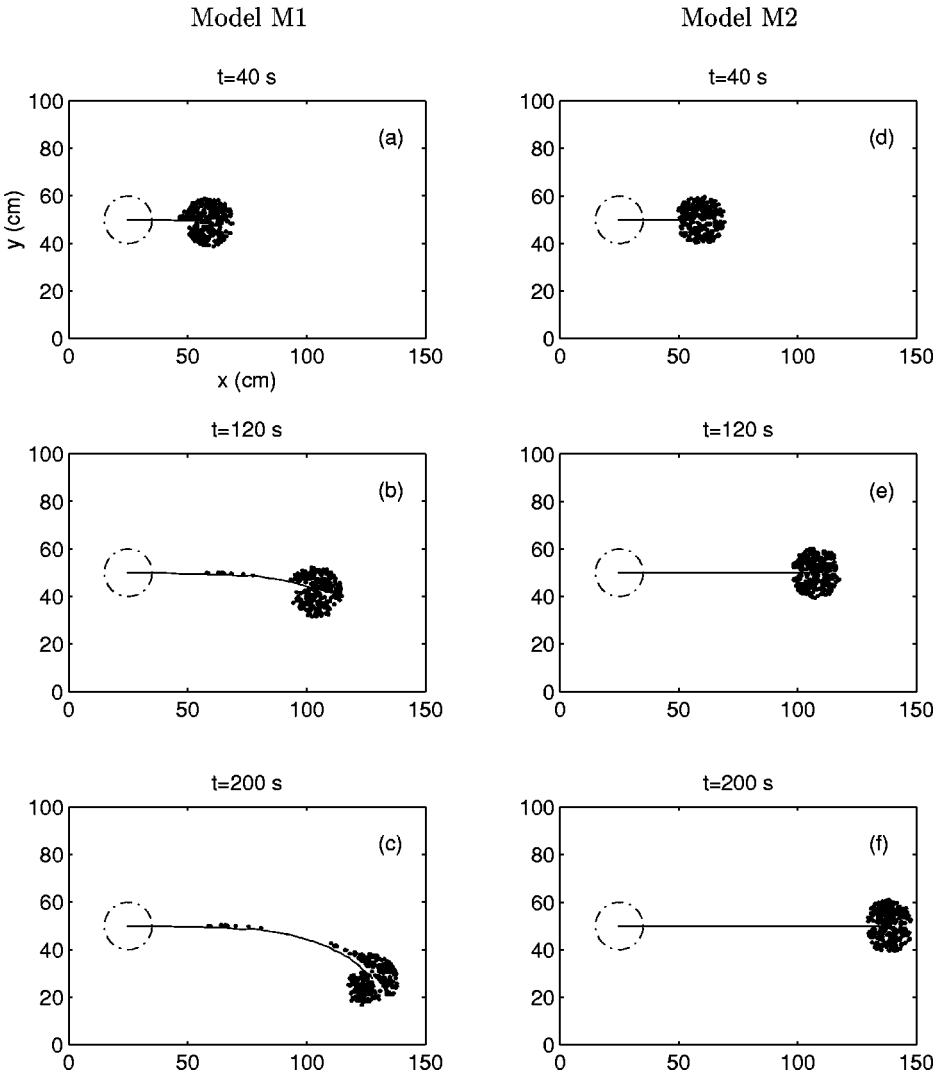

FIG. 6. Evolution of 300 tracers placed in the initial atmosphere of the dipole (indicated by the dashed–dotted circle) in (a)–(c) simulation 1, and (d)–(f) simulation 2. The tracers evolution is presented for the same times as in Fig. 1.

start of an experiment in order to ensure that the fluid has reached a state of solid body rotation. A dipolar vortex was produced by applying the same technique as described by Velasco Fuentes and van Heijst:[7] A bottomless thin-walled cylinder of about 8 cm diameter was slowly moved in the x direction, while gradually lifting it. As a result, a columnar dipole is formed in the wake of the cylinder. The relative translation motion of the cylinder has to be very slow (typically less than 5 cm s^{-1}) in order to ensure a quasi-2D motion. The flow was visualized by adding fluorescent dye to the fluid inside the cylinder before starting the experiment; the evolving dye distributions were recorded with a corotating camera mounted at some distance above the rotating tank.

Figure 10 shows the evolution of a typical dipole for the case of a mean fluid depth of 16 cm. A qualitative comparison can be made with Figs. 6(a)–6(c). Clearly, the vortex trajectory is also deflected to the right. More remarkable, the elongated shape of the cyclonic part of the dipole, together with the leaking of fluid to the ambient, are evident for $t = 160-200$ s. Before these times, the visible tail of the dipole appears as an unavoidable consequence of the experimental method. It has to be stressed that the comparison between the experimental results and the numerical simulations is only qualitative. The close resemblance between both, however, strongly suggests that the physical effects introduced in model M1 provide a much better description of the experimental evolution of the dipole than the conventional model M2.

Quantitative comparisons have not been made because the parabolic free surface, always present in the rotating tank experiments, is not included in model M1. The parabolic shape of the surface (also equivalent to the so-called γ-effect) induces stretching effects on fluid columns due to changes in depth, which eventually affect the dipole motion.[9,16] As the vortex moves towards the center of the tank, the anticyclonic part decays slower due to squeezing of fluid columns and, as a result, a deflection to the right in the vortex trajectory is also produced. The combined effect of Ekman friction plus topographic variations on barotropic flow is beyond the scope of the present study. This problem is examined separately in a different study (in progress), in which the physical model M1 is further extended in order to include variable topography.

The influence of the free surface is enhanced for lower depths because the relative change in depth in such cases is

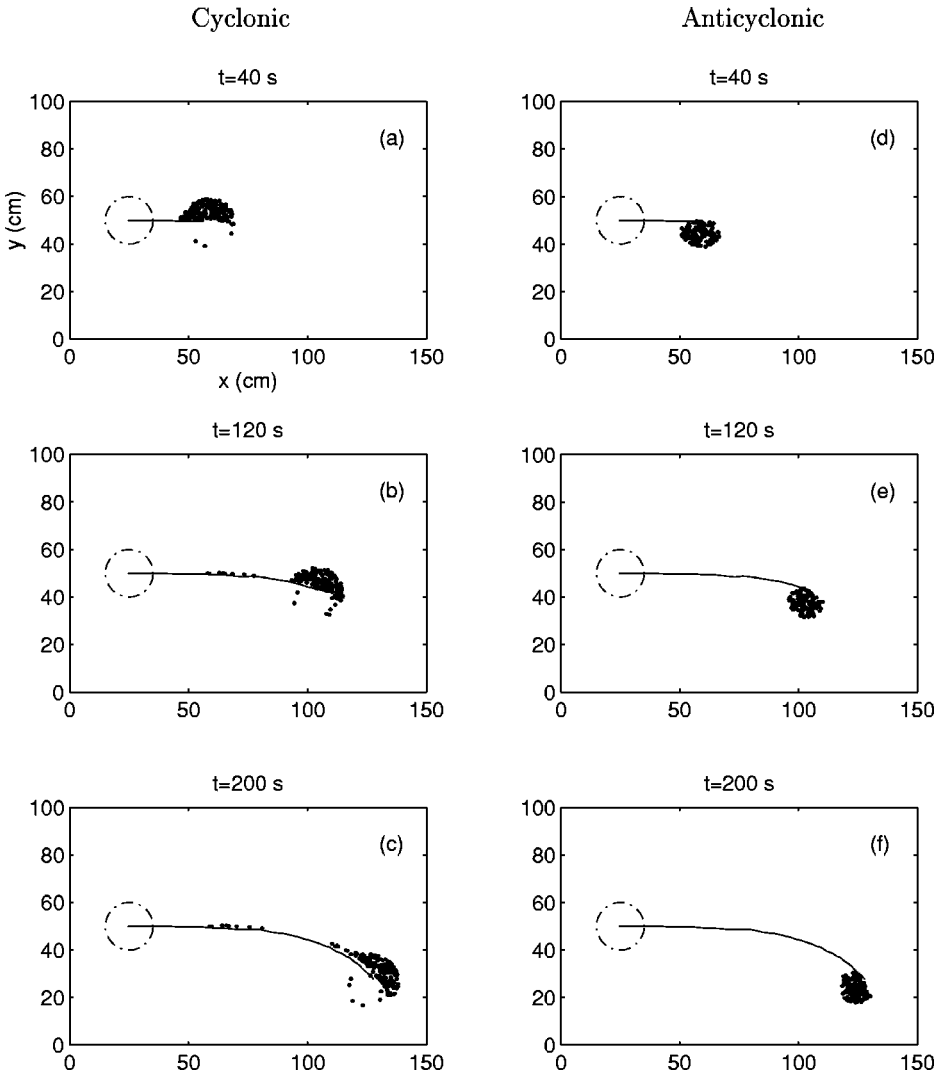

FIG. 7. Calculated evolution of passive tracers in the cyclonic (left column) and the anticyclonic (right column) halves of the dipole in simulation 1 [Figs. 6(a)–6(c)]. This figure shows that only the cyclonic part of the dipolar vortex shows detrainment when using model M1.

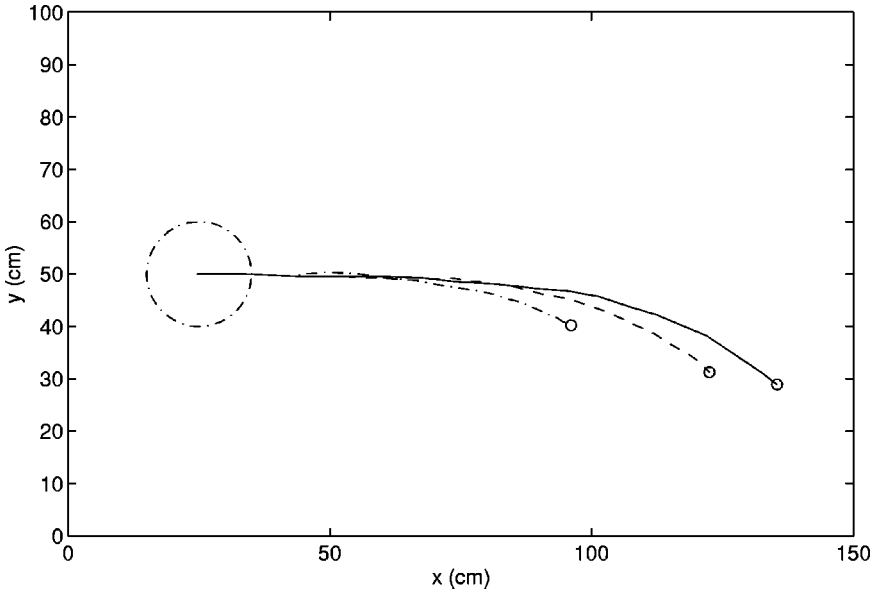

FIG. 8. Calculated dipole trajectories in numerical simulations based on model M1, using different depths (simulations 6, 1, and 5) during 180 s: $H=8$ cm (dashed–dotted line), $H=16$ cm (dashed line), $H=24$ cm (solid line). The end points are indicated by the small circles.

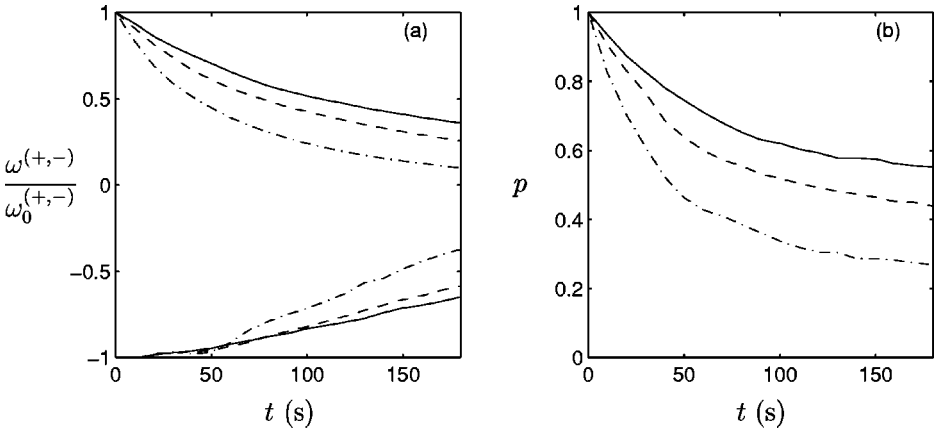

FIG. 9. (a) Time evolution of the dipole peak vorticities ω^+ and ω^- in simulations 6, 1, and 5. (b) Time evolution of the ratio $p=\omega^+/|\omega^-|$. Lines as in Fig. 8.

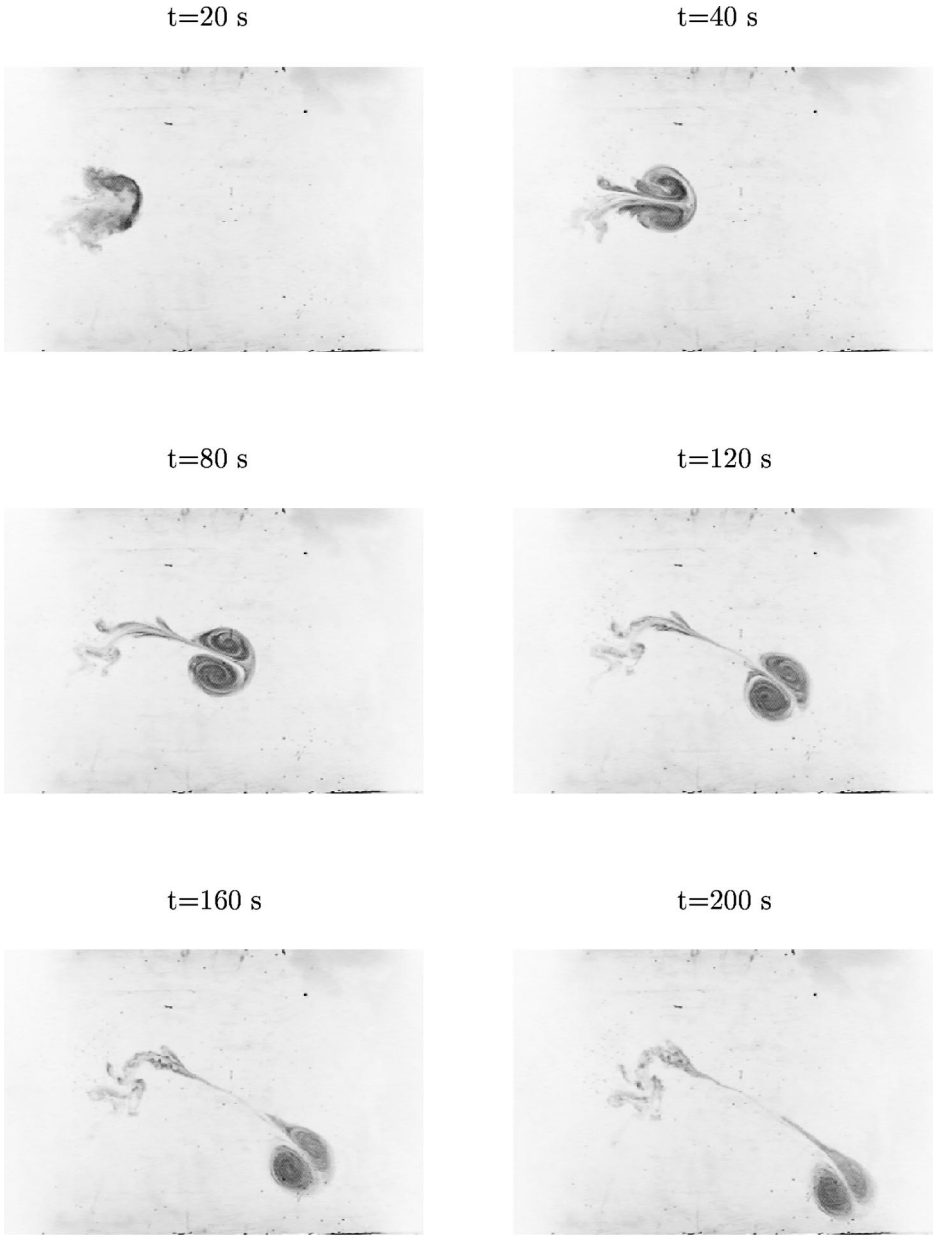

FIG. 10. Top view photographs showing the evolution of an experimental dipole during a timespan of 200 s ($0.88T_E$). The experimental parameters approximately correspond to those in numerical simulation 1.

greater. This was verified by observing the evolution of dipolar vortices in experiments where the mean depth was 8 cm (not shown here). In these cases, the dipole deviation to the right was more pronounced than in the numerically calculated trajectory shown in Fig. 8. For a mean depth of 16 cm, however, free-surface curvature effects are smaller than the bottom friction effects, and the deflected dipole trajectory observed in simulation 1 [Figs. 1(a)–1(c)] agrees with that observed in the laboratory experiment shown in Fig. 10.

V. SUMMARY AND DISCUSSION

The evolution of quasi-2D dipolar vortices over a flat bottom in a rotating system has been studied numerically. The results are qualitatively verified by means of laboratory experiments in a rotating tank. Dipolar vortices are self-propelled by the mutual interaction between their counter-rotating parts, until they collide with a boundary or until they have decayed by viscous effects. Our aim in the paper has been to examine the dipole decay during a relatively long timespan $[O(T_E)]$ in order to appreciate the effect of bottom friction. For this purpose, the numerical simulations are based on a 2D physical model derived in ZS00 [model M1, Eq. (2.1)]. This model retains the nonlinear terms associated with the linear Ekman condition at the solid bottom, in the vorticity equation. Such a model is an extension of the conventional 2D formulation, which includes Ekman effects only by a linear stretching term [model M2, Eq. (2.6)].

For the purely inviscid case, dipoles drift in a straight line maintaining the symmetry between both halves.[3] When only lateral viscosity is included [model M3, Eq. (2.7)], the dipole still moves along a straight trajectory while now gradually decaying and radially expanding.[4,5] With linear Ekman effects but without lateral viscosity [model M4, Eq. (2.8)], the dipole maintains the straight trajectory while exponentially decaying. When both lateral viscous effects and linear Ekman friction are included (model M2) the symmetry is still conserved, i.e., both halves decay at the same rate, and the dipole still moves along a rectilinear path; the decay rate is now of course larger than in models M3 and M4. The differences when using nonlinear Ekman damping, the extended model M1, are remarkable. The main results are the following: (1) the dipole trajectory is deflected towards the right (i.e., in an anticyclonic sense) and, (2) during the decay process, the cyclonic half is elongated and leaks fluid to the ambient, leaving a tail behind the dipole.

The dipole trajectory is deflected because the decay rate of the anticyclonic part is smaller than that of the cyclonic one. This effect is due to the nonlinear Ekman terms in model M1, in particular the nonlinear Ekman stretching term. This can be shown by considering model M1, Eq. (2.1) with only Ekman stretching terms,

$$\frac{\partial \omega}{\partial t} = -\frac{1}{2} E^{1/2} \omega(\omega + f). \tag{5.1}$$

When only the linear part is considered the vorticity decays exponentially as in model M4 [see the corresponding equation for ω in Table II in the Appendix]. Obviously, the vorticity decay does not depend on the sign of ω. In contrast, when the nonlinear term is included the decay is larger for $\omega > 0$ than for $\omega < 0$. This can be shown from the solution of (5.1),

$$\omega = \frac{\omega_0 \exp(-t/T_E)}{(\omega_0/f)[1-\exp(-t/T_E)]+1}, \tag{5.2}$$

where ω_0 is the initial vorticity distribution. The faster decay of cyclonic fluid columns has been pointed out in previous studies by several authors.[1,2,17,18]

The advection of fluid from the cyclonic part of the dipole to the ambient is related with the asymmetrical evolution of the vortex. Fluid from the positive part is eventually detrained from the dipole, due to its faster decay compared with the negative part. An analogous phenomenon occurs for dipolar vortices moving across isolines of ambient vorticity, as shown by Velasco Fuentes *et al.*,[8] who studied advection properties of dipoles on a topographic β-plane. Note from Fig. 7 that there has also been some exchange of fluid from the cyclonic part to the anticyclonic one. Since the scope of this study has been to show the leaking effect associated to nonlinear Ekman friction, the quantitative measurement of the advection properties is left for a more detailed study.

The main results reported in this paper were verified qualitatively by means of laboratory experiments in a rotating tank. The deflection of the vortex trajectory, the deformation of the cyclonic half, and the detrainment of dipole fluid to the ambient as seen in the numerical simulations are also clearly observed in the laboratory experiment (see Fig. 10). A quantitative comparison between experiments and simulations could not be made because of the effect of the parabolic free surface under experimental conditions, which is not accounted for in the numerical simulations. This effect (the so-called γ-effect), although weak, is expected to have an influence on the dipole trajectory.

ACKNOWLEDGMENTS

L.Z.S. gratefully acknowledges financial support from the Consejo Nacional de Ciencia y Tecnología (CONACYT, México) and from the Eindhoven University of Technology (TUE). Critical comments and reading of the manuscript by Maurice Satijn are sincerely appreciated.

APPENDIX: DIPOLE EVOLUTION IN MODEL M2

In this appendix the evolution of the Chaplygin–Lamb dipole using model M2 is analytically described. The dipole decay when using models M3 and M4 has been reported before by Nielsen and Juul Rasmussen[4] and Swaters and Flierl,[6] respectively. Since model M2 is just a combination of the viscous effects in M3 and M4, the same method of Nielsen and Juul Rasmussen is followed here. Considering the smallness of viscous effects the dipole is assumed to keep its functional form while decaying. That is, the inviscid dipole solution (3.2) is still considered valid, with the atmosphere radius a and the speed U slowly varying in time. This assumption is reinforced by observing that the scatter plot for model M2 [Fig. 5(b)] presents a closely linear relationship between ω and ψ'. The product ak is also assumed to be

constant (equal to 3.8317, being the first zero of the Bessel function J_1), which simply implies that k is a function of time as well. Note from Fig. 5(a) that these basic assumptions are clearly not valid for model M1. Obviously, the results obtained here for model M2 can be applied for model M3 (by neglecting Ekman effects) and for M4 (by neglecting lateral viscosity). Table II summarizes the evolution equations for the three models.

When considering model M2, the temporal evolution of the kinetic energy K and enstrophy S is given by

$$\frac{dK}{dt} = -2\nu S - \frac{2}{T_E}K, \tag{A1}$$

$$\frac{dS}{dt} = -2\nu \int\int (\nabla\omega)^2 dx dy - \frac{2}{T_E}S. \tag{A2}$$

The terms proportional to ν represent lateral viscosity and those proportional to T_E^{-1} represent linear Ekman friction. The enstrophy decay is obtained by multiplying Eq. (2.6) with ω and integrating over the horizontal domain. Similarly, the energy decay comes from multiplying the 2D momentum equations with the velocity vector;[4] the term associated with Ekman friction, however, was chosen analogous to the second term in the enstrophy decay. These expressions are valid for any flow vanishing at the boundaries. The energy and enstrophy of the Chaplygin–Lamb dipole are

$$K = 2\pi a^2 U^2, \tag{A3}$$

$$S = \pi\gamma^2 U^2, \tag{A4}$$

where $\gamma = ak$ is considered constant (3.8317). Assuming $U = U(t)$ and $a = a(t)$ the time evolution of K and S is

$$\frac{dK}{dt} = 4\pi a U\left(a\frac{dU}{dt} + U\frac{da}{dt}\right), \tag{A5}$$

$$\frac{dS}{dt} = 2\pi\gamma^2 U\frac{dU}{dt}. \tag{A6}$$

On the other hand, using (A3) and (A4) in Eqs. (A1) and (A2) [together with the dipole solution (3.2) in order to evaluate the integral in (A2)], it is verified that

TABLE II. Approximate solutions of the local and global properties during the dipole evolution using models M2, M3, and M4.

	M2	M3	M4
$a(t)$	$(\nu\gamma^2 t + a_0^2)^{1/2}$	$(\nu\gamma^2 t + a_0^2)^{1/2}$	a_0
$U(t)$	$U_0\left(\frac{a_0}{a}\right)^2 \exp\left(-\frac{t}{T_E}\right)$	$U_0\left(\frac{a_0}{a}\right)^2$	$U_0 \exp\left(-\frac{t}{T_E}\right)$
ω	$\omega_0\left(\frac{a_0}{a}\right)^2 \exp\left(-\frac{t}{T_E}\right)$	$\omega_0\left(\frac{a_0}{a}\right)^2$	$\omega_0 \exp\left(-\frac{t}{T_E}\right)$
$K(t)$	$K_0\left(\frac{a_0}{a}\right)^2 \exp\left(-\frac{2t}{T_E}\right)$	$K_0\left(\frac{a_0}{a}\right)^2$	$K_0 \exp\left(-\frac{2t}{T_E}\right)$
$S(t)$	$S_0\left(\frac{a_0}{a}\right)^4 \exp\left(-\frac{2t}{T_E}\right)$	$S_0\left(\frac{a_0}{a}\right)^4$	$S_0 \exp\left(-\frac{2t}{T_E}\right)$

$$\frac{dK}{dt} = -2\pi\nu\gamma^2 U^2 - \frac{4\pi}{T_E}a^2 U^2, \tag{A7}$$

$$\frac{dS}{dt} = -2\pi\nu\gamma^4\frac{U^2}{a^2} - \frac{2\pi}{T_E}\gamma^2 U^2. \tag{A8}$$

Combining (A6) with (A8), and afterwards (A5) with (A7) yields the evolution equations for U and a^2,

$$\frac{dU}{dt} = -\left(\frac{\nu\gamma^2}{a^2} + \frac{1}{T_E}\right)U, \tag{A9}$$

$$\frac{d(a^2)}{dt} = \nu\gamma^2. \tag{A10}$$

After time integration,

$$a(t) = (\nu\gamma^2 t + a_0^2)^{1/2}, \tag{A11}$$

$$U(t) = U_0\left(\frac{a_0^2}{\nu\gamma^2 t + a_0^2}\right)\exp\left(-\frac{t}{T_E}\right), \tag{A12}$$

where the subindex 0 denotes the value at $t=0$. Since it has been assumed that $\omega = k^2\psi'$, the vorticity evolution is given by

$$\frac{\partial\omega}{\partial t} = -\left(\nu k^2 + \frac{1}{T_E}\right)\omega; \tag{A13}$$

using $k^2(t) = \gamma^2/a^2(t)$ the solution is

$$\omega(x,y,t) = \omega_0(x,y)\left(\frac{a_0^2}{\nu\gamma^2 t + a_0^2}\right)\exp\left(-\frac{t}{T_E}\right). \tag{A14}$$

The corresponding expressions for the global quantities K and S [using (A3) and (A4)] are

$$K(t) = 2\pi a_0^2 U_0^2\left(\frac{a_0^2}{\nu\gamma^2 t + a_0^2}\right)\exp\left(-\frac{2t}{T_E}\right), \tag{A15}$$

$$S(t) = \pi\gamma^2 U_0^2\left(\frac{a_0^4}{(\nu\gamma^2 t + a_0^2)^2}\right)\exp\left(-\frac{2t}{T_E}\right). \tag{A16}$$

Equations (A11), (A12), and (A14)–(A16) describe the temporal dipole evolution according to model M2. The corresponding analytical expressions for models M3 and M4 are easily obtained by setting $T_E \to \infty$ (model M3) or $\nu = 0$ and T_E fixed (model M4), as shown in Table II. In order to facilitate the comparison the evolution equations are rewritten by using $K_0 = 2\pi a_0^2 U_0^2$ and $S_0 = \pi\gamma^2 U_0^2$, the initial energy and enstrophy values of the Chaplygin–Lamb dipole. Note that the dipole's atmosphere is unchanged when model M4 is considered. Thus, obviously, the evolution of $a(t)$ is the same in models M2 and M3.

Figure 11 shows the temporal evolution of ω, U, K, and S calculated from simulations based on M2, M3, and M4, already presented in Sec. III A, but now compared with the analytical expressions in Table II. Note that the energy and enstrophy (which can be called ''global'' properties, since they involve spatial integrations over the whole domain)

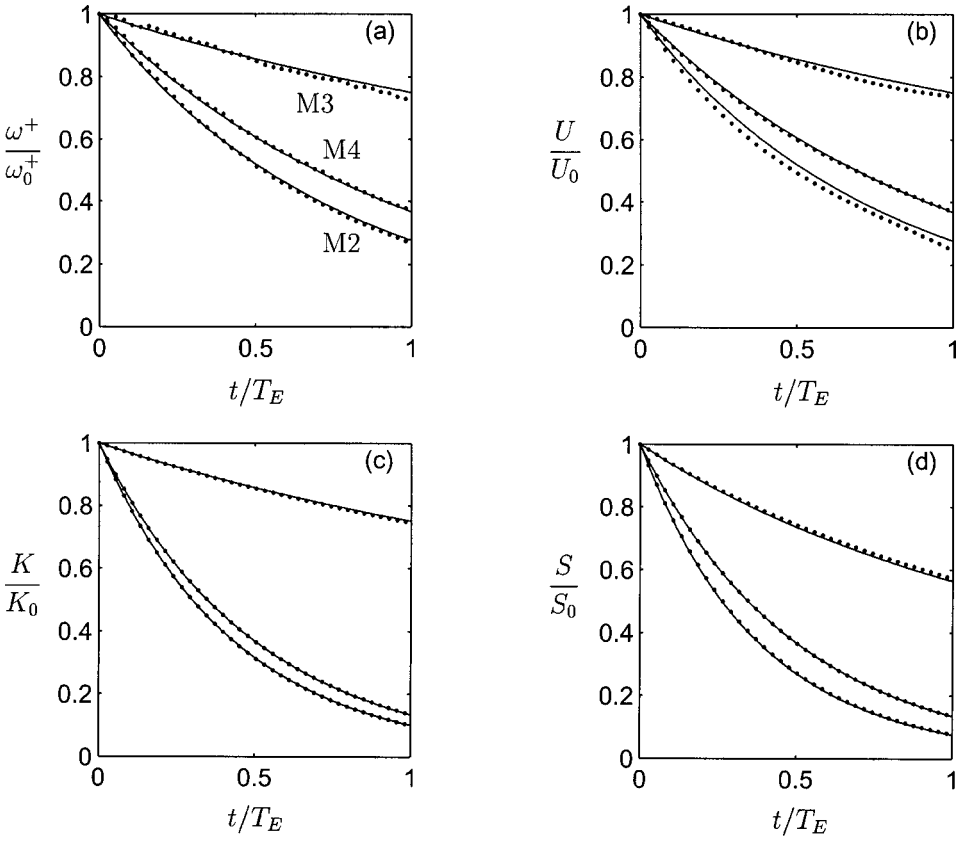

FIG. 11. Temporal evolution of (a) ω^+, (b) U, (c) K, and (d) S calculated from simulations 2, 3, and 4 (dotted lines) compared with their corresponding analytical expressions in Table II (solid lines). The dipole decay is more pronounced when using model M2, while the slowest decay occurs for model M3.

have an excellent agreement with the predicted values for the three models. The ''local'' properties U and ω (in this case, the peak vorticity ω^+ of the cyclonic part) also show a similar evolution to the numerically calculated values, although the accuracy is lower. The analytical values of these properties are slightly overestimated for models M2 and M3, while M4 yields a better result [see, e.g., Fig. 11(b)]. This indicates that the assumption of a linear $\omega-\psi'$ relationship during the evolution slightly fails when lateral viscous effects are taken into account. This is mainly due to the lateral diffusion of vorticity, present in M2 and M3, and not in M4.

[1]L. Zavala Sansón and G. J. F. van Heijst, ''Nonlinear Ekman effects in rotating barotropic flows,'' J. Fluid Mech. **412**, 75 (2000).
[2]R. C. Kloosterziel and G. J. F. van Heijst, ''The evolution of stable barotropic vortices in a rotating free-surface fluid,'' J. Fluid Mech. **239**, 607 (1992).
[3]V. V. Meleshko and G. J. F. van Heijst, ''On Chaplygin's investigation of two-dimensional vortex structures in an inviscid fluid,'' J. Fluid Mech. **272**, 157 (1994).
[4]A. H. Nielsen and J. Juul Rasmussen, ''Formation and temporal evolution of the Lamb-dipole,'' Phys. Fluids **9**, 982 (1997).
[5]J. H. G. M. van Geffen and G. J. F. van Heijst, ''Viscous evolution of 2D dipolar vortices,'' Fluid Dyn. Res. **22**, 191 (1998).
[6]G. E. Swaters and R. G. Flierl, ''Ekman dissipation of a barotropic modon,'' in *Mesoscale/Synoptic Coherent Structures in Geophysical Turbulence*, edited by J. C. J. Nihoul and B. M. Jamart (Elsevier, Amsterdam, 1989).
[7]O. U. Velasco Fuentes and G. J. F. van Heijst, ''Experimental study of dipolar vortices on a topographic β-plane,'' J. Fluid Mech. **259**, 79 (1994).
[8]O. U. Velasco Fuentes, G. J. F. van Heijst, and B. E. Cremers, ''Chaotic transport by dipolar vortices on a β-plane,'' J. Fluid Mech. **291**, 139 (1995).
[9]O. U. Velasco Fuentes, ''Propagation and transport properties of vortices on a γ-plane,'' Phys. Fluids **6**, 3341 (1994).
[10]G. F. Carnevale, O. U. Velasco Fuentes, and P. Orlandi, ''Inviscid dipole–vortex rebound from a wall or coast,'' J. Fluid Mech. **351**, 75 (1997).
[11]J. Pedlosky, *Geophysical Fluid Dynamics*, 2nd ed. (Springer-Verlag, New York, 1987).
[12]P. Orlandi, ''Vortex dipole rebound from a wall,'' Phys. Fluids A **2**, 1429 (1990).
[13]J. H. G. M. van Geffen, *NS-evol*. Internal report R-1466-D, Fluid Dynamics Laboratory, Department of Physics, Eindhoven University of Technology, The Netherlands.
[14]L. Zavala Sansón and G. J. F. van Heijst, ''Interaction of barotropic vortices with coastal topography: Laboratory experiments and numerical simulations,'' J. Phys. Oceanogr. **30**, 2141 (2000).
[15]L. Zavala Sansón, G. J. F. van Heijst, and J. J. J. Doorschot, ''Reflection of barotropic vortices from a step-like topography,'' Nuovo Cimento Soc. Ital. Fis., C **22**, 909 (1999).
[16]O. U. Velasco Fuentes, G. J. F. van Heijst, and N. P. M. Lipzig, ''Unsteady behavior of a topography-modulated tripole,'' J. Fluid Mech. **307**, 11 (1996).
[17]R. C. Kloosterziel, ''Barotropic vortices in a rotating fluid,'' Ph.D. thesis, University of Utrecht, 1990.
[18]G. J. F. van Heijst, R. C. Kloosterziel, and C. W. M. Williams, ''Laboratory experiments on the tripolar vortex in a rotating fluid,'' J. Fluid Mech. **225**, 301 (1991).